Biosensors and Bioelectronics 113 (2018) 39–45

Contents lists available at ScienceDirect

Biosensors and Bioelectronics

journal homepage: www.elsevier.com/locate/bios

Discrimination of single nucleotide mismatches using a scalable, flexible, and transparent three-dimensional nanostructure-based plasmonic miRNA sensor with high sensitivity

Hee-Kyung Na[a], Jung-Sub Wi[a], Hye Young Son[b], Jong G. Ok[c], Yong-Min Huh[b], Tae Geol Lee[a,*]

[a] Center for Nano-Bio Measurement, Korea Research Institute of Standards and Science (KRISS), Daejeon 34113, Republic of Korea
[b] Department of Radiology, College of Medicine, Yonsei University, Seoul 03722, Republic of Korea
[c] Department of Mechanical and Automotive Engineering, Seoul National University of Science and Technology, Seoul 01811, Republic of Korea

ARTICLE INFO

Keywords:
LSPR biosensor
miRNA sensing
Scalable plasmonic nanostructure
Single base mismatch discrimination

ABSTRACT

Localized surface plasmon resonance (LSPR) biosensors have attracted much interest due to their capacity for multiplexing, miniaturization, and high performance, which offers the potential for their integration into lab-on-a-chip platforms for point-of-care (POC) diagnostics. The need for microRNA (miRNA)-sensing platforms is particularly urgent because miRNAs are key regulators and biomarkers in numerous pathological processes and diseases. Unfortunately, however, development of such miRNA-sensing platforms has not yet been achieved. In order to realize the detection of these important biomarkers, there has been an increasing demand for POC-sensing platforms that enable label-free quantification with low sample consumption, good sensitivity, real-time responsiveness, and high throughput. Here, we developed a highly specific, sensitive LSPR miRNA-sensing platform on a flexible, scalable plasmonic nanostructure to enable single-base mismatch discrimination and attomole detection of miRNAs in clinically relevant samples. The hairpin probe contained a locked nucleic acid (LNA) that enabled the discrimination of single base mismatches based on differences in melting temperatures of perfectly matched or single base mismatched miRNAs when they formed base pairs with probes. In addition, through hybridization induced signal amplification based on precipitate formation on the gold surface through the enzyme reaction, we observed a dramatic LSPR peak shift, which enabled attomole detection. Additionally, our LSPR miRNA sensor enabled the detection of *miR-200a-3p* in total RNA extracts from primary cancer cell lines without purification or labeling of the miRNA. This label-free and highly specific miRNA sensing platform may have applications in POC cancer diagnostics without the need for gene amplification.

1. Introduction

MicroRNAs (miRNAs) are endogenous, noncoding RNAs that are short in length (19–22 nt) and involved in numerous biological processes (Bartel, 2004; Zhang et al., 2007; Ambros, 2004). The expression of various miRNAs is associated with a wide range of diseases, including cancer, neurodegenerative disorders, and diabetes (Lu et al., 2005; Calin and Croce, 2006; Esquela-Kerscher and Slack, 2006; Liu et al., 2012; Brennan et al., 2017). Hence, the accurate detection of the expression levels of one or more miRNAs could facilitate their wide-ranging applications as diagnostic and prognostic biomarkers (Kanwal et al., 2017; Jang et al., 2017; Dou et al., 2017; Jones et al., 2012). However, their low abundance in biofluids, fragile structure, small size, and sequence similarity among family members have been vexing impediments to the development of ultrasensitive and highly specific sensing platforms (Hunt et al., 2015; Catuogno et al., 2011).

Various miRNA detection methods, including real-time quantitative polymerase chain reaction (PCR), fluorescence, and electrochemical sensing platforms, have been developed; however, these methods require amplification and labeling, and are hindered by difficulties in quantitative detection when using clinically relevant samples (Lee et al., 2015; Ryoo et al., 2013; Su et al., 2016; Tian et al., 2013). As such, there has been an increased demand for platforms that enable quantitative miRNA sensing without labeling and amplification and that can be easily implemented and developed into point-of-care (POC) diagnostic systems (Cardoso et al., 2016; Dorvel et al., 2012; Pang et al., 2016). In addition, for practical bioanalytical and clinical applications using cell extracts, the miRNA biosensors must exhibit reproducible signal generation, high specificity capable of single-base mismatch discrimination, high-throughput capability for simultaneous detection

* Corresponding author.
E-mail address: tglee@kriss.re.kr (T.G. Lee).

https://doi.org/10.1016/j.bios.2018.04.033
Received 8 February 2018; Received in revised form 6 April 2018; Accepted 16 April 2018
Available online 22 April 2018

of various targets and samples, and high sensitivity (Xiao et al., 2009a; Xiao et al., 2009b; Wei et al., 2016; Huang et al., 2015).

Localized surface plasmon resonance (LSPR) biosensors exploit a phenomenon in which the binding of an analyte to the surface of a nanostructure induces a change in the local refractive index, resulting in a wavelength shift (Lee et al., 2011; Sepúlveda et al., 2009). As a result, LSPR biosensors are able to facilitate sensitive and label-free quantification of biomolecules using simple instrumentation (Mayer et al., 2008; Yang et al., 2016). Moreover, they offer the potential for multiplexed, miniaturized assays with straightforward implementation and high performance that can be applied to lab-on-a-chip or POC devices (Song et al., 2017); Park et al., 2017). Chip-based LSPR biosensors have advantages over platforms that consist of colloidal nanoparticles because their use allows the user to avoid the tedious washing/centrifugation process without being concerned about stability in the buffers and biological samples (Guo et al., 2017). The fabrication strategy utilized to obtain three-dimensional (3D) plasmonic nanostructures on large-scale substrates for integration into various types of lab-on-a-chip and high-throughput sensing platforms must be cost-effective, reproducible, flexible, and scalable (Thilsted et al., 2016; Stewart et al., 2008). Thus, much effort has been made to fabricate 3D plasmonic nanostructures that satisfy these requirements (Verellen et al., 2011; Cetin and Altug, 2012; Wi et al., 2013). For practical applications, the fabrication strategy should also be straightforward. Because accurate disease diagnosis and prognosis depend on determining the type and stage of the specific disease, it is important that the miRNAs be detected and quantified with high accuracy, sensitivity, and throughput (Tian et al., 2012; Wong et al., 2015; Li et al., 2014; Labib et al., 2013). In this study, we offer a new strategy to produce a highly sensitive LSPR miRNA sensing platform that is capable of single-base mismatch discrimination on a flexible, scalable 3D plasmonic nanostructure. For the 3D plasmonic nanostructure, we fabricated uniform gold strips on a 4-in.-scale substrate through a simple, cost-effective procedure. To generate a distinguishable, reproducible, large LSPR peak shift in the presence of the target miRNA, a signal amplification strategy using a well-designed probe structure was utilized, resulting in a device with high performance and sequence specificity.

2. Materials and methods

2.1. Electromagnetic simulation

Electromagnetic simulations were performed using two-dimensional (2D) finite-difference time-domain software (Lumerical FDTD solution 8.9). To calculate the absorbance curves, a simulation mesh was set to a 0.1-nm square grid. The refractive indices of the substrate and organic layer were assumed to be constants of 1.5 and 1.6, respectively. To simulate the arrayed nanostructures, a perfectly matched layer was used as the boundary condition for the *z*-axis, and periodic boundary conditions with 200 nm periodicity were used for the *x*- and *y*-axes. The modeled structure in a uniform dielectric medium (n = 1.33) was illuminated from the top with a linearly polarized plane wave.

2.2. SAM formation

The sequences for the miRNAs, hairpin probes, and signaling probes are available in the supplementary information section. Wafer-sized plasmonic nanopatterns were cut into small pieces, fitted in a cuvette or 16-well chamber and the small pieces of patterns were washed with ethanol and water. Synthesized LNA probes were diluted to 10 μM concentration in phosphate-buffered saline (PBS) and annealed at 95 °C for 5 min with a gradual temperature decrease down to 4 °C. A solution of the thiol-modified and annealed probe in PBS was introduced to the gold nanopattern with the same concentration of 3-mercapto-1-propanol and incubated overnight. The sensor modified with the probe was washed with PBS five times.

2.3. Detection of miRNA

The sensor modified with a probe was treated with a predetermined concentration of miRNA in buffer (or in total RNA dissolved in PBS) overnight at room temperature. For miRNA detection in total RNA, extracted total RNA was quantified using Take3 plates in SynergyH1 (Biotek, UK) and dissolved in PBS. Then, the mixture was incubated in 70 °C for 1 h and followed by washing with PBS three times at 70 °C for 10 min. After washing, the sensor in PBS was cooled down to 4 °C. The signal sequence shown above was dissolved in PBS at a concentration of 500 nM and was applied to the sensor. After incubation for 3 h, the sensor was washed with PBS three times, and incubated with 1% bovine serum albumin (BSA) in the PBS for 1 h. Streptavidin-horseradish peroxidase (HRP) conjugate solution in 1% BSA in PBS was added to the sensor at a concentration of 25 μg/mL for 1 h. After repeated washing with PBS, the sensor was incubated with a mixture of 980 μL of 4-chloronaphthol solution and 20 μL of 100 mM H_2O_2 for 10 min. Absorbance spectra of plasmonic sensors were obtained using a UV–vis spectrophotometer (UV-2600; Shimadzu, Japan) or microplate reader (SynergyH1; Biotek, Winooski, VT, USA).

3. Results and discussion

3.1. Fabrication of 3D plasmonic nanostructure

Fig. 1 depicts the signal amplification strategy used to accurately detect miRNAs on 3D nanostructures on gold strips. Briefly, the 3D plasmonic gold nanostructure was fabricated via roll-to-roll nanoimprint lithography (R2R NIL) followed by Au deposition (Wi et al., 2017; Ahn and Guo, 2009). The Au strips were then formed by thermal evaporation of gold with a deposition angle of 35° on polyurethane acrylate (PUA) nanogratings obtained by R2R NIL using a polydimethylsiloxane mold to generate the 200-nm period and 100-nm nanograting pattern. In our tests, the Au strips provided the potential for high-throughput analysis (Fig. S1a), and the flexible, transparent 3D nanostructure conferred benefits related to easy integration in various types of lab-on-a-chip and POC diagnostic devices. In addition, the inverted “L” shape of the gold nanostructures obtained by Au deposition on the top and sidewall surfaces of the PUA nanogratings (using a controlled oblique deposition angle) enabled the formation of a surface plasmon with a long oscillation length, which is known to have enhanced refractive index sensitivity compared to the rod-shaped Au deposited structure at the top (Miller and Lazarides, 2005; Larsson et al., 2007; Kazuma and Tatsuma, 2014). The 3D gold nanostructures were characterized by scanning electron microscopy (SEM) and ultraviolet-visible spectroscopy. SEM images indicate that our nanofabrication facilitated the formation of uniform patterns and a unique gold deposited structure, as shown in Fig. 2a. The absorbance curve showed characteristics of plasmonic nanostructures in phosphate-buffered saline (PBS), as shown in Fig. 2b. Two characteristic peaks were observed at the wavelengths of 760 nm and 605 nm, which originate from the oscillation of the surface plasmon of the entire Au strip and the oscillation of the surface plasmon in the internal segments of the line array such as the Au film on the top, respectively.

3.2. Signal amplification for miRNA detection

To obtain an easily distinguishable and reproducible LSPR peak shifts in buffer, the signal amplification strategy used was based on precipitate formation of the substrate via an enzymatic reaction. To induce target-specific precipitate formation, our probe was designed to have a hairpin structure that consisted of a fully complementary sequence against the target, causing a conformational change to the double-stranded form in the presence of a fully matched target molecule, accompanied by thermal destabilization of a partially hybridized sequence with mismatched miRNA. The probe was further designed to

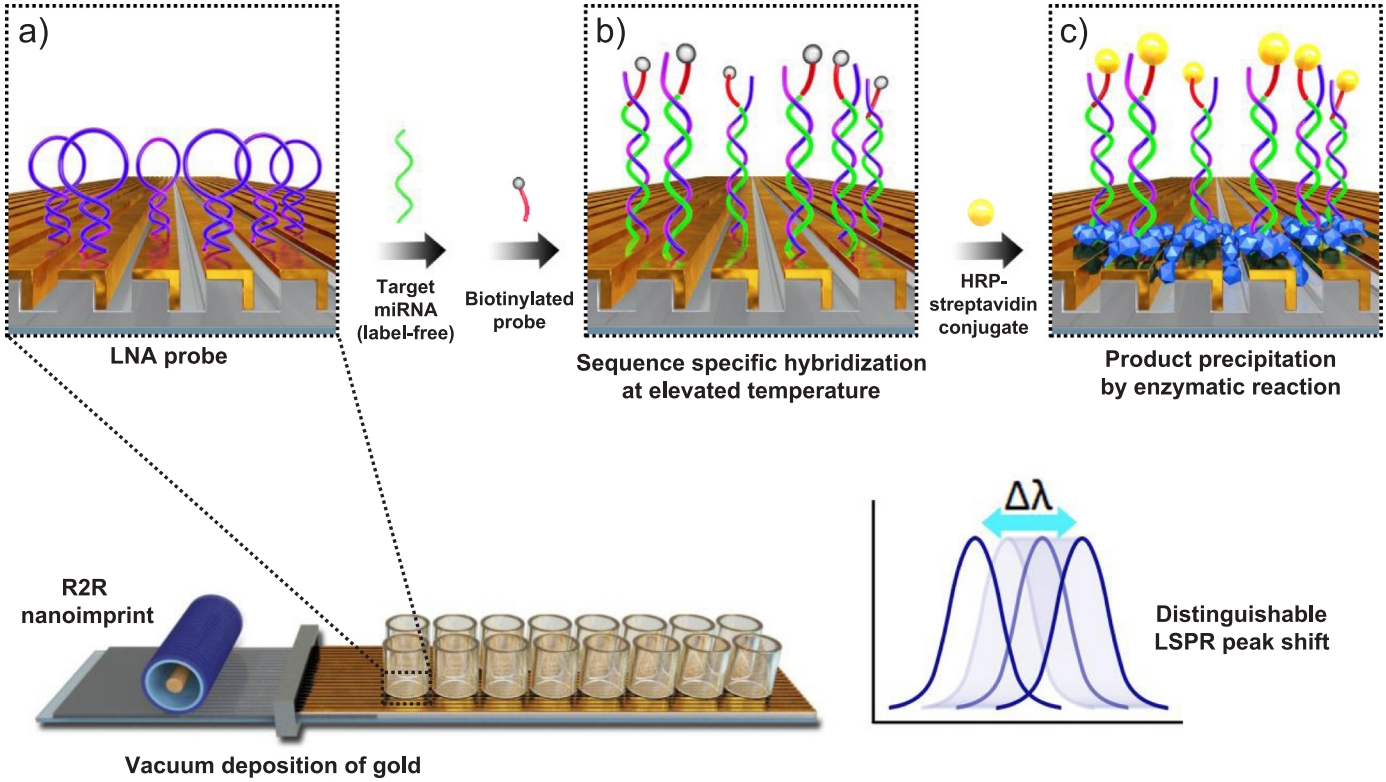

Fig. 1. Schematic of the signal-amplified LSPR miRNA sensing platform on a scalable, flexible, transparent three-dimensional (3D) plasmonic nanostructure. a) Self-assembled monolayer (SAM) formation with a hairpin LNA probe, b) hybridization with miRNAs at elevated temperature followed by treatment with a biotinylated signaling probe, and c) binding with HRP-streptavidin followed by enzymatic reaction converting soluble substrate to insoluble precipitate.

allow the binding of a horseradish peroxidase (HRP)-streptavidin conjugate to a biotin-labeled signal sequence to trigger the conversion of the soluble substrate into an insoluble precipitate in the presence of the target miRNA. In addition, locked nucleic acid (LNA), which forms a covalent bond between the 2′ oxygen and 4′ carbon of the ribose ring, was chosen as a probe due to its enhanced affinity to complementary RNA, enabling the discrimination of single-base mismatches (You et al., 2004; Owczarzy et al., 2011; Braasch and Corey, 2001). To demonstrate the usefulness of our strategy in detecting clinically relevant miRNAs, we chose the *let-7* miRNA family as a target miRNA because they contain a perfectly matched target (*let-7a*) and single nucleotide-substituted targets (*let-7c* and *let-7f*) to observe the ability of our sensor to detect single base mismatches, as well as *miR-200a*, which is a known prognostic and diagnostic cancer biomarker (Li et al., 2015; Matsuura et al., 2016; Meng et al., 2016; Masood and Yasmin, 2017).

To predict the feasibility of our strategy, the LSPR peak shift was estimated by a calculation that used a two-dimensional finite difference time domain (FDTD) simulation according to changes in the surrounding organic layer. In the FDTD simulation, 30-nm-thick gold strips (100 nm wide at the top and 120 nm in height) were modeled as a function of thickness of the organic layer. The calculated spectra exhibited noticeable peak shifts that depended on the thickness of the organic layer on the Au strips, suggesting that the LSPR biosensor could be designed to generate a large absorbance peak shift by controlling target-specific insoluble precipitate formation (Fig. 2c–e).

To assess the performance of our LSPR miRNA sensor, the annealed thiol-terminated hairpin LNA probe and mercapto-propanol were introduced onto the Au strips, followed by conformational changes upon hybridization in the presence of the target miRNA. The hybridization-induced binding of the biotin-containing signal sequence further triggered the enzyme-based precipitation of 4-chloronaphthol by the HRP-streptavidin conjugate, which is commonly used in enzyme-linked immunosorbent assays (ELISAs) and other biological assays. Since hybridization alone barely induces a distinguishable LSPR peak shift due to small changes in the refractive index (particularly in buffer), signal amplification was required for reproducible and sensitive analyte sensing (Fig. S2) (Elhadj et al., 2004). In addition, LPSR changes of even several nanometers often cause poor reproducibility and accuracy in measurements and data interpretation, particularly with instrumentation used for high-throughput analysis (Wang and Tang, 2015; Xu et al., 2016). However, because enzymatic precipitation of the substrate was controlled in a target-specific manner, our LSPR sensor showed a large peak shift (up to 37 nm) in the presence of 100 nM *let-7a* in PBS in Fig. 3a. SEM images shown in Fig. 3c and d provide decisive evidence of precipitate formation in the presence of miRNA compared with the observed line pattern in the absence of miRNA (Fig. S3). Furthermore, precipitate formation occurred uniformly over a large area, indicating successful formation of a self-assembled monolayer and hybridization with target miRNA over the entire area of the gold pattern (Fig. S4). In addition, the sensing platform produced a concentration-dependent LSPR peak shift, as shown in Fig. 3b. Using various concentrations of miRNA samples in buffer, the limit of detection (LOD) was calculated as 13 fM (2.6 attomole in 200 μL) according to the following equation: LOD = 3.3 (SD / S), where SD is the standard deviation, and S is the slope of the calibration curve (Fig. S5). Thus, our signal amplification strategy on the gold nanostructure enabled sensitive target detection in a buffer solution based on reproducible signal generation with a distinguishable LSPR shift. Since our signal amplification strategy resulted in a large LSPR shift in buffer with high sensitivity comparable to previous reports (Johnson and Mutharasan, 2014), our miRNA sensing platform has a large potential in overcoming the issue of reproducibility.

3.3. Discrimination of single base mismatches

Next, we investigated the single-base mismatch discrimination

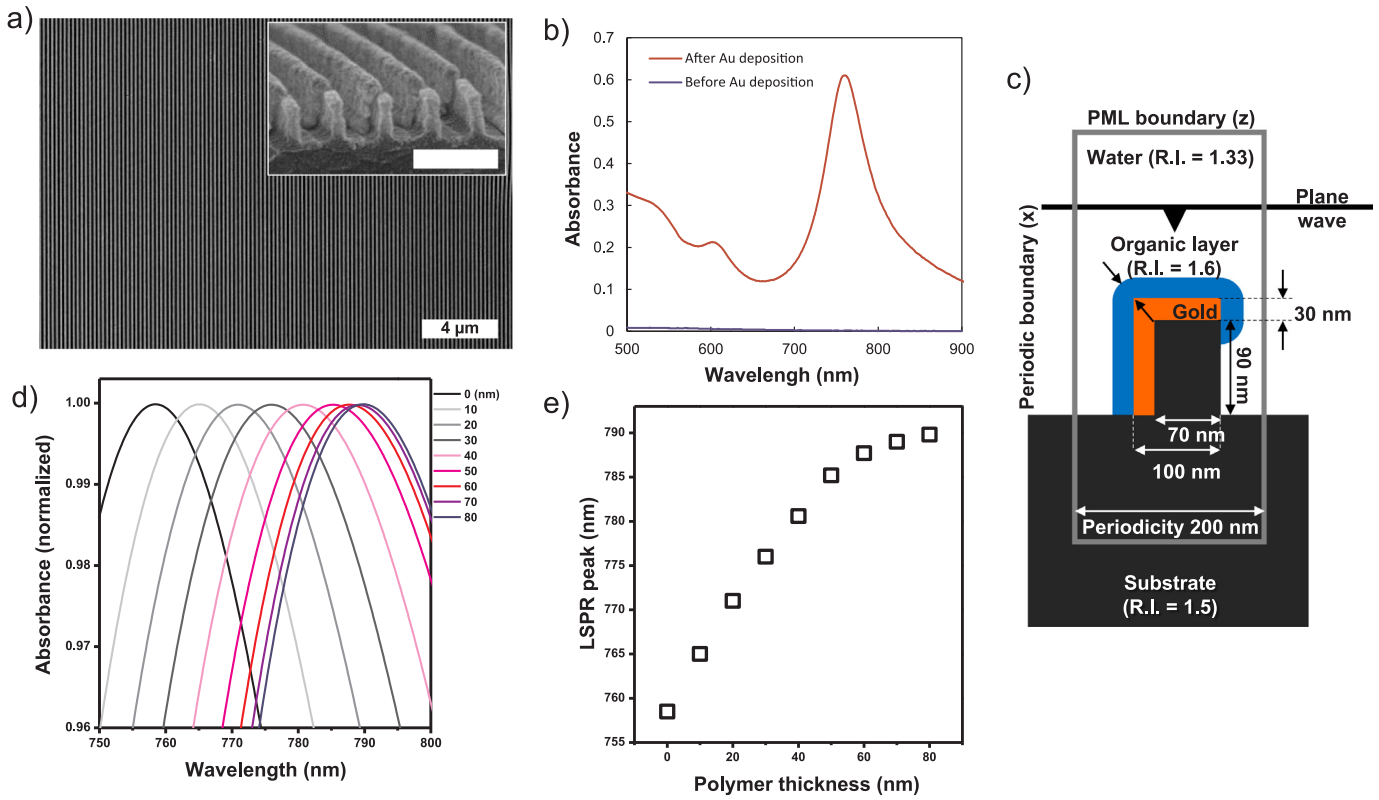

Fig. 2. Characterization of the 3D gold nanostructure obtained by angled Au deposition on transparent polymer nanograting (a, b) and FDTD simulation for formation of an organic layer on the 3D gold nanostructure for modeling the enzyme substrate precipitation in the presence of target miRNA (c–e). (a) SEM images of gold patterns. Scale bar: 4 μm (inset: 400 nm). (b) Measured absorbance spectrum of the 3D gold nanostructure in PBS. Blue line: absorbance spectrum of line array before Au deposition, and red line: absorbance spectrum after Au deposition. (c) Schematic illustration of the cross-sectional view for the FDTD simulation. (d, e) FDTD simulation results. (For interpretation of the references to color in this figure legend, the reader is referred to the web version of this article.).

capability of our sensor to assess the sequence specificity for target miRNA. The ability to discriminate single base mismatches is important, as many miRNAs have sequence similarities among different short miRNA (Roush and Slack, 2008; Qiu et al., 2014). The *miR-let-7* family of miRNAs was chosen to investigate the potential of our sensor to discriminate between mismatched sequences. We checked the sensor performance with respect to the LSPR shift in the presence of *miR-let-7a* as a perfectly matched target as well as *miR-let-7c* and let-7f, which contain single nucleotide differences in their sequences (Fig. 4a and b). Single-base mismatch discrimination was achieved through incubation and washing at 70 °C, resulting in denaturation of the thermally unstable base pairing between the LNA probe and mismatched miRNA. Interestingly, no significant changes were observed in the presence of *miR-let-7c* and *miR-let-7f* compared with the large LSPR peak shift that was observed with *miR-let-7a*, revealing that our LSPR sensor was capable of sequence-specific recognition of a perfectly matched target (Fig. 4a). Because of the observed discrimination between *miR-let-7* family members, our LNA-modified LSPR sensor has the potential to be a platform for highly specific miRNA sensing to distinguish nonspecific sequences containing only a single nucleotide substitution.

3.4. miRNA detection in a 16-well chamber

We then examined the applicability of our sensor for high-throughput analysis. Our 3D gold nanostructure was processed into a 4-in. wafer-scale substrate, and a multi-well format was easily produced. In a 16-well chamber format, we were able to perform the same procedure described above and measure the LSPR peak changes using a microplate reader (Fig. S1b). The data showed a remarkable LSPR peak shift in a miRNA concentration-dependent manner. Thus, we found that our system worked in a multi-well format for use with a microplate reader, indicating its potential use for high-throughput analyses with various POC diagnostic devices based on their scalable and flexible nanofabrication strategies. Because of well-established microfluidic systems, our flexible and scalable plasmonic nanostructure possesses great potential to be integrated into lab-on-a-chip-based diagnostic devices for further improved performance.

3.5. miRNA detection in total RNA extracts from primary cancer cell lines

For diagnostic and prognostic applications, the sensitive detection of miRNAs from biologically relevant samples is essential, and while total RNA can be easily extracted from cells, tissues, or other biological samples, direct detection of a target miRNA from total RNA without amplification is difficult due to its low abundance and sequence similarity in a complex system. With this background, we tested miRNA detection from cell extracts using our sensor. To investigate the sensor performance in biological samples, two different human primary gastric cancer cell lines (MKN45 and SNU1) were chosen based on their *miR-200a-3p* expression levels, as determined by qRT-PCR. Prior to the detection of miRNA from cell extracts, we compared the sensor performance in the presence of spiked-in 10 nM miRNAs in buffer or a total RNA mixture. The treatment containing *miR-200a-3p* in buffer or a total RNA sample isolated from SNU1 cells induced a similar LSPR peak shift, indicating that the hairpin probe could be hybridized with target miRNA without interference in the presence of large amounts of nonspecific RNAs (0.04% of spiked-in miRNA in total RNA in the sample, Fig. S6).

Finally, we examined whether the sensor could be utilized to detect a target in a biological sample. We observed a specific and distinguishable LSPR peak shift on modified Au strips that were complementary to *miR-200a-3p* in total RNA extracts from *miR-200a-3p*-

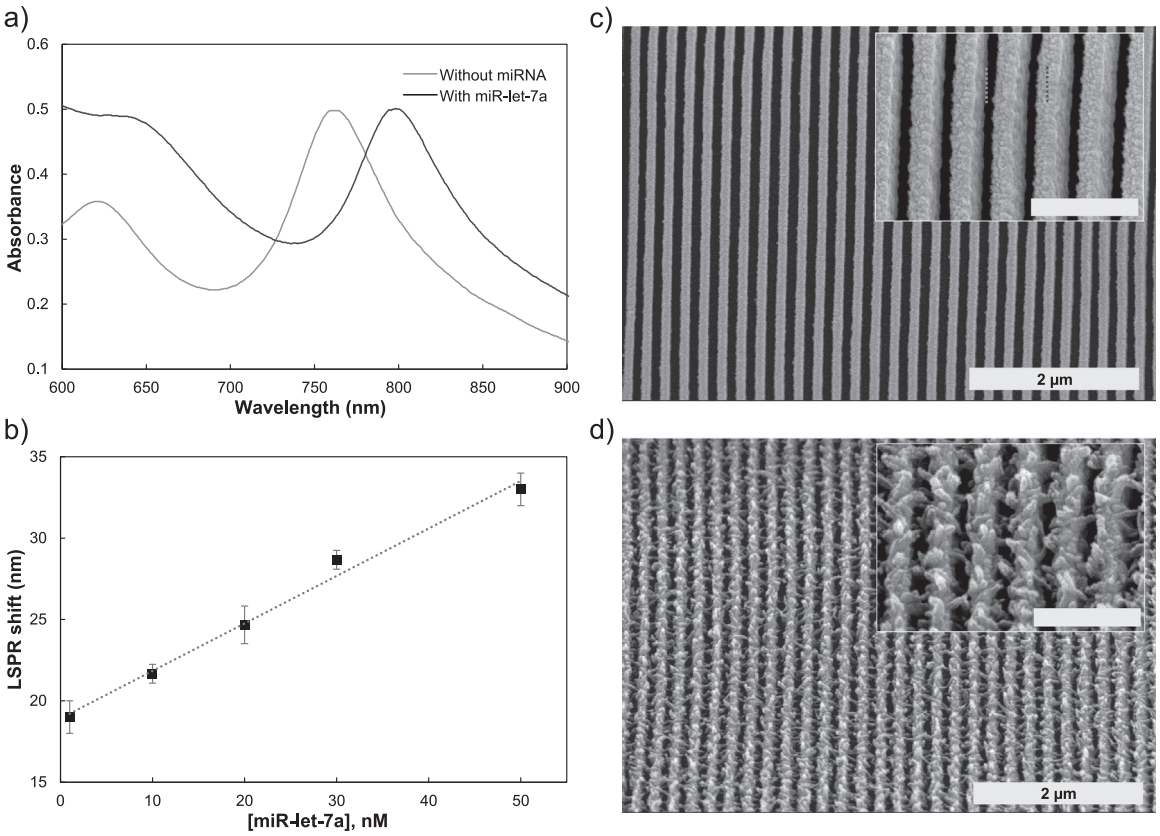

Fig. 3. Sensitivity of the LSPR miRNA-sensing platform on the gold line pattern in buffer. (a) LSPR spectra of patterns after incubation in the absence (gray) or presence of target miRNA (black). (b) Concentration-dependent LSPR shifts in the presence of *miR-let-7a*. (c, d) SEM images of Au strips after enzyme substrate precipitation in the absence (c) and presence (d) of target miRNA. Scale bar: 2 μm (inset: 500 nm).

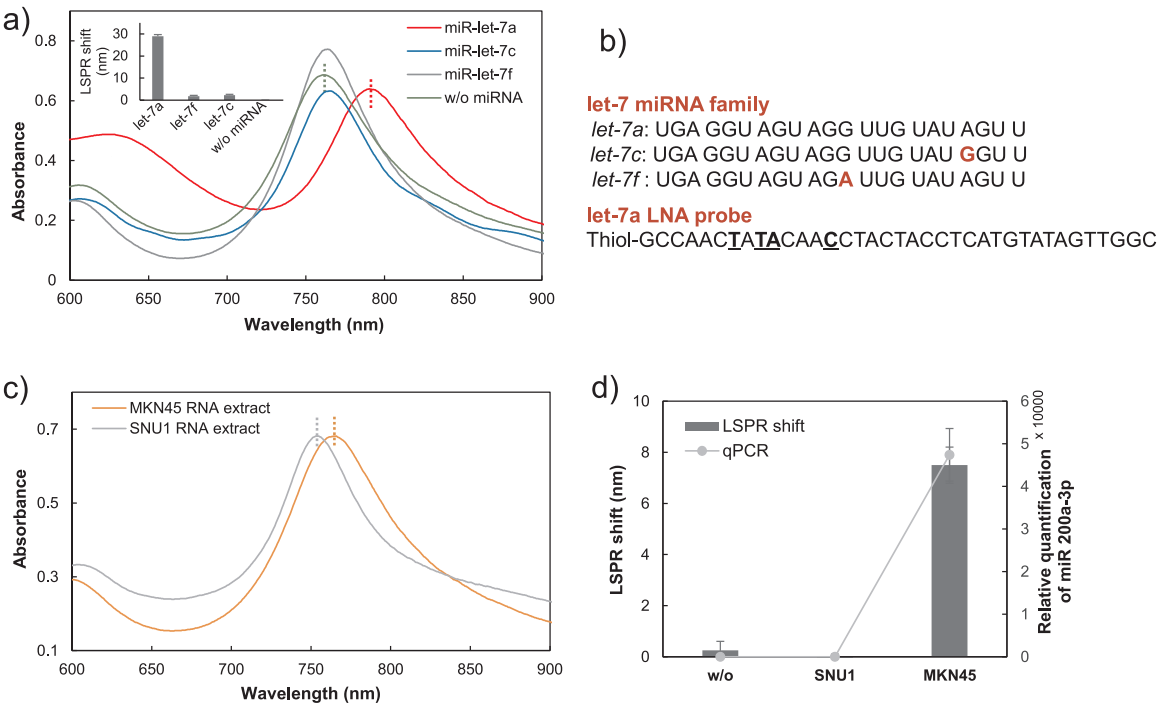

Fig. 4. Sequence specificity of the LSPR sensor for miRNA. (a) LSPR spectra of the pattern after incubation in the absence (green) or presence of *miR-let-7c* (blue), *miR-let-7f* (gray), or *miR-let-7a* (red, 25 nM each). (b) Probe sequence for *miR-let-7a* detection and sequences of *miR-let-7a*, *miR-let-7c*, and *miR-let-7f*. Mismatch positions in miRNA sequences are in red. LNA positions are underlined and in bold. (c) *miR-200a-3p* detection in total RNA extracts from human stomach adenocarcinoma cells. (d) LSPR peak shift in total RNA from human primary gastric cancer cells expressing (MKN45) and not expressing (SNU1) *miR-200a-3p* and quantification of *miR-200a-3p* in each cell line by qRT-PCR. (For interpretation of the references to color in this figure legend, the reader is referred to the web version of this article.).

expressing MKN45 cells, but not SNU1 cells that did not express *miR-200a-3p*, consistent with the qRT-PCR results (Fig. 4c and d). These results have implications for miRNA detection and quantification, since many RNAs in total RNA extracts can interfere with the hybridization of a probe with its target by competitive binding of molecules having sequence similarity, thereby reducing the sensitivity and specificity of the sensor. However, our sensor exhibited target-specific sensing in the presence of numerous structurally similar RNA molecules in biological samples.

4. Conclusion

In conclusion, we have demonstrated a new strategy for ultrasensitive LSPR sensing of miRNA with high sequence specificity on a straightforward, scalable, flexible, and transparent 3D plasmonic nanostructure. Signal amplification strategy together with the use of an LNA-modified probe resulted in a distinguishable LSPR peak shift and attomole detection of miRNA as well as single base mismatch discrimination without labeling, reverse transcription, or gene amplification, which are required steps in qRT-PCR. To the best of our knowledge, our platform showed the largest signal changes ever observed in an LSPR miRNA sensor. In addition, our platform appeared to be well suited for clinical applications of biomarker detection. We believe that our LSPR miRNA sensing platform will broaden the applicability of LSPR biosensors as simple, portable, and low-cost POC devices for personalized prognostic and diagnostic miRNA profiling. However, since the analysis time of our LSPR miRNA sensing platform is still too long to use for direct application as a POC diagnostic tool in clinical applications, we are currently working to shorten the analysis time to within 1–2 h by integrating LSPR miRNA analysis platform into a microfluidic device and using a reaction cocktail based on nanomaterials.

Acknowledgments

The work was supported by the Development of Platform Technology for Innovative Medical Measurements Program (KRISS-2018-GP2018-0018) from the Korea Research Institute of Standards and Science, the Nano Material Technology Development Program (NRF-2014M3A7B6020163), the Bio & Medical Technology Development Program (NRF-2015M3A9D7029894), and the Global Frontier Project (H-GUARD_2013M3A6B2078962) of the National Research Foundation (NRF) funded by the Ministry of Science and ICT and Development of Nanotechnology-based Quantitative Surface Mass Spectrometric Platform Technique to Detect Low-mass Biomolecules funded by the MOTIE.

Conflicts of interest

There are no conflicts of interest to declare.

Contributions

H.-K. Na, J.-S. Wi, Y. M. Huh, and T. G. Lee designed the research. H.-K. Na, J.-S. Wi, H.Y. Son, and J.G. Ok performed the experiments, analyzed the data, and discussed the results. All of the authors contributed to the writing of this manuscript, and all of the authors have given their approval to the final version of the manuscript

Appendix A. Supporting information

Supplementary data associated with this article can be found in the online version at http://dx.doi.org/10.1016/j.bios.2018.04.033.

References

Ahn, S.H., Guo, L.J., 2009. ACS Nano 3, 2304–2310.
Ambros, V., 2004. Nature 431, 350–355.
Bartel, D.P., 2004. Cell 116, 281–297.
Braasch, D.A., Corey, D.R., 2001. Chem. Biol. 8, 1–7.
Brennan, E., Wang, B., McClelland, A., Mohan, M., Marai, M., Beuscart, O., Derouiche, S., Gray, S., Pickering, R., Tikellis, C., De Gaetano, M., Barry, M., Belton, O., Ali-Shah, S.T., Guiry, P., Jandeleit-Dahm, K.A.M., Cooper, M.E., Godson, C., Kantharidis, P., 2017. Diabetes 66, 2266–2277.
Calin, G.A., Croce, C.M., 2006. Nat. Rev. Cancer 6, 857–866.
Cardoso, A.R., Moreira, F.T.C., Fernandes, R., Sales, M.G.F., 2016. Biosens. Bioelectron. 80, 621–630.
Catuogno, S., Esposito, C.L., Quintavalle, C., Cerchia, L., Condorelli, G., de Franciscis, V., 2011. Cancers 3, 1877–1898.
Cetin, A.E., Altug, H., 2012. ACS Nano 6, 9989–9995.
Dorvel, B.R., Reddy, B., Go, J., Duarte Guevara, C., Salm, E., Alam, M.A., Bashir, R., 2012. ACS Nano 6, 6150–6164.
Dou, Z., Lin, S., Dai, C., Lu, Y., Tian, T., Wang, M., Liu, X., Zheng, Y., Xu, P., Li, S., Sheng, Q., Deng, Y., Dai, Z., 2017. Oncotarget 8, 62703–62715.
Elhadj, S., Singh, G., Saraf, R.F., 2004. Langmuir 20, 5539–5543.
Esquela-Kerscher, A., Slack, F.J., 2006. Nat. Rev. Cancer 6, 259–269.
Guo, L., Jackman, J.A., Yang, H.-H., Chen, P., Cho, N.-J., Kim, D.-H., 2017. Nano Today 10, 213–239.
Huang, S., Romero-Ruiz, M., Castell, O.K., Bayley, H., Wallace, M.I., 2015. Nat. Nanotechnol. 10, 986–991.
Hunt, E.A., Broyles, D., Head, T., Deo, S.K., 2015. Annu. Rev. Anal. Chem. 8, 217–237.
Jang, M.H., Kim, H.J., Gwak, J.M., Chung, Y.R., Park, S.Y., 2017. Hum. Pathol. 68, 69–78.
Johnson, B.N., Mutharasan, R., 2014. Analyst 139, 1576–1588.
Jones, K.B., Salah, Z., Del Mare, S., Galasso, M., Gaudio, E., Nuovo, G.J., Lovat, F., LeBlanc, K., Palatini, J., Randall, R.L., Volinia, S., Stein, G.S., Croce, C.M., Lian, J.B., Aqeilan, R.I., 2012. Cancer Res. 72, 1865–1877.
Kanwal, R., Plaga, A.R., Liu, X., Shukla, G.C., Gupta, S., 2017. Cancer Lett. 407, 9–20.
Kazuma, E., Tatsuma, T., 2014. Nanoscale 6, 2397–2405.
Labib, M., Khan, N., Ghobadloo, S.M., Cheng, J., Pezacki, J.P., Berezovski, M.V., 2013. J. Am. Chem. Soc. 135, 3027–3038.
Larsson, E.M., Alegret, J., Kall, M., Sutherland, D.S., 2007. Nano Lett. 7, 1256–1263.
Lee, J., Park, G., Min, D.-H., 2015. Chem. Commun. 51, 14597–14600.
Lee, S.-W., Lee, K.-S., Ahn, J., Lee, J.-J., Kim, M.-G., Shin, Y.-B., 2011. ACS Nano 5, 897–904.
Li, S., Wang, X., Gu, Y., Chen, C., Wang, Y., Liu, J., Hu, W., Yu, B., Wang, Y., Ding, F., Liu, Y., Gu, X., 2015. Mol. Ther. 23, 423–433.
Li, X., Ni, M., Zhang, C., Ma, W., Zhang, Y., 2014. RNA 20, 252–259.
Liu, N., Landreh, M., Cao, K., Abe, M., Hendriks, G.-J., Kennerdell, J.R., Zhu, Y., Wang, L.-S., Bonini, N.M., 2012. Nature 482, 519–523.
Lu, J., Getz, G., Miska, E.A., Alvarez-Saavedra, E., Lamb, J., Peck, D., Sweet-Cordero, A., Ebert, B.L., Mak, R.H., Ferrando, A.A., Downing, J.R., Jacks, T., Horvitz, H.R., Golub, T.R., 2005. Nature 435, 834–838.
Masood, N., Yasmin, A., 2017. Pathol. Oncol. Res. 23, 707–715.
Matsuura, K., De Giorgi, V., Schechterly, C., Wang, R.Y., Farci, P., Tanaka, Y., Alter, H.J., 2016. Hepatology 64, 732–745.
Mayer, K.M., Lee, S., Liao, H., Rostro, B.C., Fuentes, A., Scully, P.T., Nehl, C.L., Hafner, J.H., 2008. ACS Nano 2, 687–692.
Meng, X., Müller, V., Milde-Langosch, K., Trillsch, F., Pantel, K., Schwarzenbach, H., 2016. Oncotarget 7, 16923–16935.
Miller, M.M., Lazarides, A.A., 2005. J. Phys. Chem. B 109, 21556–21565.
Owczarzy, R., You, Y., Groth, C.L., Tataurov, A.V., 2011. Biochemistry 50, 9352–9367.
Pang, Y., Wang, C., Wang, J., Sun, Z., Xiao, R., Wang, S., 2016. Biosens. Bioelectron. 79, 574–580.
Park, Y., Ryu, B., Oh, B.-R., Song, Y., Liang, X., Kurabayashi, K., 2017. ACS Nano 11, 5697–5705.
Qiu, X., Wang, P., Cao, Z., 2014. Biosens. Bioelectron. 60, 351–357.
Roush, S., Slack, F.J., 2008. Trends Cell Biol. 18, 505–516.
Ryoo, S.R., Lee, J., Yeo, J., Na, H.-K., Kim, Y.-K., Jang, H., Lee, J.H., Han, S.W., Lee, Y., Kim, V.N., Min, D.-H., 2013. ACS Nano 7, 5882–5891.
Sepúlveda, B., Angelomé, P.C., Lechuga, L.M., Liz-Marzán, L.M., 2009. Nano Today 4, 244–251.
Song, Y., Chen, P., Chung, M.T., Nidetz, R., Park, Y., Liu, Z., McHugh, W., Cornell, T.T., Fu, J., Kurabayashi, K., 2017. Nano Lett. 17, 2374–2380.
Stewart, M.E., Anderton, C.R., Thompson, L.B., Maria, J., Gray, S.K., Rogers, J.A., Nuzzo, R.G., 2008. Chem. Rev. 108, 494–521.
Su, S., Wu, Y., Zhu, D., Chao, J., Liu, X., Wan, Y., Su, Y., Zuo, X., Fan, C., Wang, L., 2016. Small 13, 3794–3801.
Thilsted, A.H., Pan, J.Y., Wu, K., Zór, K., Rindzevicius, T., Schmidt, M.S., Boisen, A., 2016. Small 12, 6745–6752.
Tian, K., He, Z., Wang, Y., Chen, S.-J., Gu, L.-Q., 2013. ACS Nano 7, 3962–3969.
Tian, W., Dong, X., Liu, X., Wang, G., Dong, Z., Shen, W., Zheng, G., Lu, J., Chen, J., Wang, Y., Wu, Z., Wu, X., 2012. PLoS One 7, e29551.
Verellen, N., Van Dorpe, P., Huang, C.J., Lodewijks, K.G., Vandenbosch, A.E., Lagae, L., Moshchalkov, V.V., 2011. Nano Lett. 11, 391–397.
Wang, Y., Tang, L., 2015. Biosens. Bioelectron. 67, 18–24.
Wei, Y., Zhou, W., Li, X., Chai, Y., Yuan, R., Xiang, Y., 2016. Biosens. Bioelectron. 77, 416–420.
Wi, J.-S., Tominaka, S., Nagao, T., 2013. Adv. Opt. Mater. 1, 814–818.
Wi, J.-S., Lee, S., Lee, S.H., Oh, D.K., Lee, K.-T., Park, I., Kwak, M.K., Ok, J.G. Wi, 2017. Nanoscale 9, 1398–1402.
Wong, A.S.L., Choi, G.C.G., Cheng, A.A., Purcell, O., Lu, T.K., 2015. Nat. Biotechnol. 33, 952–961.
Xiao, Y., Plakos, K.J.I., Lou, X., White, R.J., Qian, J., Plaxco, K.W., Soh, H.T., 2009a.

Angew. Chem. Int. Ed. 48, 4354–4358.
Xiao, Y., Lou, X., Uzawa, T., Plakos, K.J.I., Plaxco, K.W., Soh, H.T., 2009b. J. Am. Chem. Soc. 131, 15311–15316.
Xu, Z., Jiang, J., Wang, X., Han, K., Ameen, A., Khan, I., Chang, T.-W., Liu, G.L., 2016. Nanoscale 8, 6162–6172.
Yang, H.-W., Tsai, R.-Y., Chen, J.-P., Ju, S.-P., Liao, J.-F., Wei, K.-C., Zou, W.-L., Hua, M.-Y., 2016. ACS Appl. Mater. Interfaces 8, 30845–30852.
You, Y., Moreira, B.G., Behlke, M.A., Owczarzy, R., 2004. Nucleic Acids Res. 34, e60.
Zhang, B., Pan, X., Cobb, G.P., Anderson, T.A., 2007. Dev. Biol. 302, 1–12.